Revised paper 567178: Dual-pumping supercontinuum generation and temporal reflection in a nonlinear photonic integrated circuit

C. KHALLOUF,[1] L. SADER,[2] A. BOUGAUD,[2] G. FANJOUX,[1]
B. LITTLE,[3] S. T. CHU,[4] D. J. MOSS,[5]
R. MORANDOTTI,[6] G. P. AGRAWAL, [7] J. M. DUDLEY,[1,8] B. WETZEL,[2]
AND T. SYLVESTRE[1,*]

[1]*Institut FEMTO-ST, CNRS UMR 6174, Université Marie et Louis Pasteur (UMLP), Besançon, France*
[2]*XLIM Research Institute, CNRS UMR 7252, Université de Limoges, Limoges, France*
[3]*QXP Technologies Inc., Xi'an, China*
[4]*Department of Physics, City University of Hong Kong, Hong Kong, China*
[5]*Optical Sciences Centre, Swinburne University of Technology, Hawthorn, Victoria, Australia*
[6]*INRS-EMT, 1650 Boulevard Lionel-Boulet, Varennes, J3X 1S2, Québec, Canada*
[7]*The Institute of Optics, NY 14627, University of Rochester, USA*
[8]*Institut Universitaire de France, Paris, France*
[*]*thibaut.sylvestre@univ-fcomte.fr*

Abstract: We report on the first demonstration of on-chip supercontinuum generation through dual-wavelength pumping of a nonlinear photonic integrated circuit, fabricated from high-index doped silica glass. In addition to the bandwidth enhancement through cross-phase modulation, we also observe multiple temporal reflections that help to extend the bandwidth further through far-detuned radiations. The experimental results show good agreement with the phase-matching theory and numerical simulations. Additionally, our real-time, pulse-to-pulse, spectral measurements through the dispersive Fourier transform technique reveal a significant increase in relative intensity noise for dual-wavelength pumping compared to the case of single-wavelength pumping.

1. Introduction

Supercontinuum (SC) generation has been a cornerstone of optical research for decades, enabling applications in metrology, imaging, spectroscopy, and telecommunications [1–7]. Traditionally, optical fibers and bulk media have dominated SC generation, achieving record bandwidths and spectral power densities spanning from the ultraviolet to the mid-infrared [7]. However, recent advancements in the design and fabrication of low-loss, highly nonlinear integrated photonic waveguides have driven growing interest in on-chip SC sources [8, 9]. The miniaturization of optical components offers significant advantages, including a reduced footprint, lower power consumption, and cost efficiency. As a result, on-chip SC generation plays a crucial role in integrated photonics, particularly in the development of octave-spanning SC for stabilized optical frequency combs [10]. SC generation has been successfully demonstrated in waveguides made from various materials, including silica (SiO_2) [11], highly-doped silica (SiON) [12], silicon (Si) [13], silicon nitride (Si_3N_4) [14–16], silicon germanium (SiGe) [17, 18], titanium dioxide (TiO_2) [19], chalcogenide glass (As_2S_3) [20], lithium niobate on insulator (LNOI) [21], Aluminum nitride (AlN) [22], and more recently Gallium arsenide (GaAs) [23]. These materials have enabled SC bandwidths extending from the visible to the mid-infrared up to 13 μm [8]. Despite these advancements, most research on photonic integrated circuits (PICs) has focused on single femtosecond-pulse pumping schemes. Expanding beyond single-pump approaches could unlock new possibilities for enhanced SC generation and broaden the scope of integrated

photonic applications.

In this work, we report on the first demonstration of on-chip SC generation in a high-index doped silica glass waveguide using dual femtosecond pumping at the 1040-nm and 1560-nm wavelengths. By leveraging the nonlinear phenomenon of cross-phase modulation (XPM), we significantly enhance the SC generation, achieving broader bandwidths and improved spectral power densities. Dual-wavelength pumping also allows us to observe spectral signatures of temporal reflections. In recent years, there has been growing interest in exploring temporal analogs of optical reflection and refraction in nonlinear waveguides [24]. It has been found that ultrashort pulses at one wavelength undergo large frequency shifts when they encounter a temporal index barrier created by pulses at another wavelength, a phenomenon closely related to the optical event horizon [25, 26]. In this study, we demonstrate multiple temporal reflections of the 1040-nm pulse interacting with a soliton-like barrier at 1560 nm. Moreover, we show that such temporal reflections extend the SC bandwidth further through generation of additional dispersive waves, opening new possibilities for integrated photonics applications. In our experiments, temporal reflections induce significant frequency shifts in the visible region, in full agreement with our numerical simulations and phase-matching theory.

2. Experiments

Dual-pumping schemes have already been implemented for photonic crystal fibers (PCFs) using pulses of widths ranging from femtoseconds to nanoseconds [27–29]. Such previous experiments have consistently shown that simultaneously pumping PCFs in their normal and anomalous dispersion regimes, using fundamental and second-harmonic signals at 1064 nm and 532 nm, respectively, results in a broader and flatter SC spectrum in the visible region as a result of XPM between the two pulses.
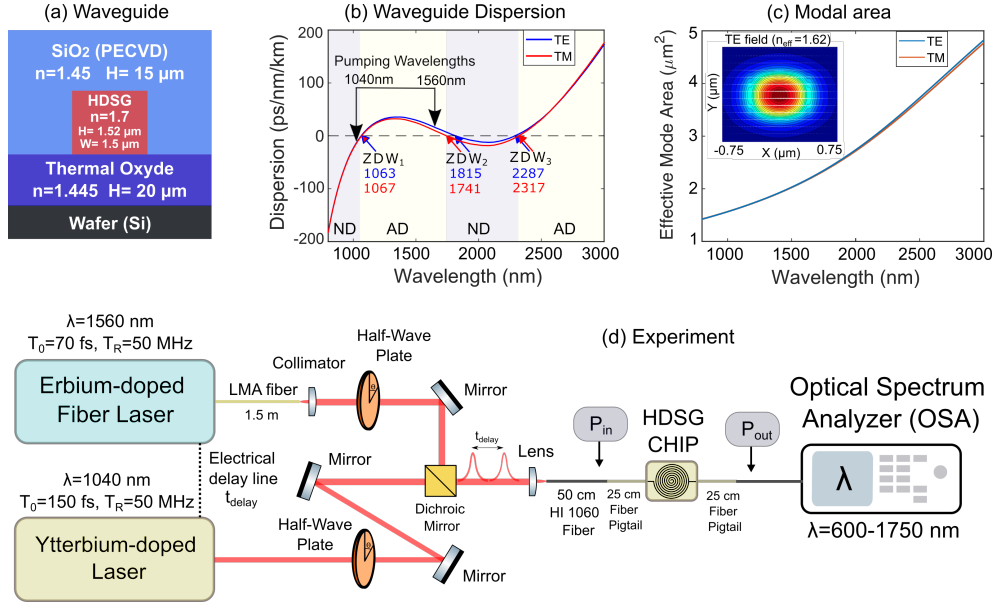

Fig. 1. (a) Cross-section of the highly doped silica glass (HDSG)waveguide fabricated by QXP technologies; (b) Wavelength dependence of the group-velocity dispersion of the waveguide for the TE and TM fundamental modes; (c) Effective mode areas versus wavelength for the same two modes; (d) Experimental setup for the dual-pumped SC generation.

In our experiments, we employ bichromatic pumping at 1040 nm and 1560 nm for a 50 cm long, spiral-shape, highly doped silica-glass (HDSG) ridge waveguide fabricated by QXP technologies [30]. The cross-section of the waveguide selected for this study is shown in Fig. 1(a). The waveguide core has dimensions of 1.5 μm x 1.52 μm, a high refractive index of n = 1.7, and a nonlinear coefficient of 250 $W^{-1}km^{-1}$ at 1560 nm. It is embedded in plasma-enhanced chemical vapor deposition (PECVD) silica (SiO_2), which is deposited on a thermal SiO_2 layer atop a silicon wafer. To characterize the waveguide's optical properties, we performed numerical simulations using a software based on the finite element method (Ansys Lumerical Mode Solutions) and computed the effective index, group-velocity dispersion (GVD), and effective mode areas for both the fundamental TE and TM modes over a wavelength range of 600 to 3000 nm. In view of slightly different refractive indices of thermal and PECVD silica, both values were used for numerical results [31] shown in Figs. 1(b) and (c). The GVD parameter D in Fig. 1(b) reveals three zero-dispersion wavelengths (ZDW) near 1064 nm, 1800 nm, and 2300 nm for the fundamental TE and TM modes. Our selected pump wavelengths, 1040 nm (close to the first ZDW) and 1560 nm in the anomalous dispersion regime, were chosen to optimize nonlinear interactions within the waveguide for temporal reflections. Fig. 1(c) presents the modal effective areas as a function of wavelength for the fundamental TE and TM modes, with the TE-mode intensity profile shown in inset. To assess propagation losses, we employed a high-resolution optical time-domain reflectometer (OBR 4600, Luna Tech.), measuring a total insertion loss of 8.9 dB at 1560 nm. The propagation loss was estimated to be as low as 0.1 dB/cm [32], indicating a high optical quality of the fabricated waveguide.

Figure 1(d) shows the experimental setup schematically. Two synchronized femtosecond fiber lasers were used for bichromatic pumping: (1) An erbium-doped fiber laser (C-Fiber 780, MenloSystems) emitting 1560 nm pulses with a full-width at half maximum (FWHM) of 70 fs at a 50 MHz repetition rate ; (2) An ytterbium-doped fiber laser (Orange Sync 50 MHz HP3, MenloSystems) emitting 1040 nm pulses with a width of 150 fs and an average output power of 4 W in free space, also operating at the 50 MHz repetition rate. The 1560-nm pre-chirped laser output is coupled into a 1.5-m-long large-mode-area (LMA) polarization-maintaining fiber, ensuring linear polarization while minimizing nonlinear effects caused by its high average power of 120 mW. The 1040-nm fiber laser, with a high output power of 4 W, is attenuated to 200 mW using a half-wave plate and a polarization beam splitter to prevent waveguide damage. A collimator at the LMA fiber output ensures efficient free-space propagation. The polarization angles of both laser pulses (linearly polarized) are precisely adjusted using half-wave plates (HWPs) to maximize their nonlinear interactions. Several mirrors are used for spatial alignment, and a dichroic mirror (Thorlabs - DMSP1180) ensures co-propagation of 1560 nm pulses with the 1040 nm pulses. The combined beams are coupled into single-mode fibers connected to the chip waveguide using an aspherical lens. The coupling fibers consist of a 25-cm polarization-maintaining (PM) single-mode fiber (SMF) pigtail glued to the chip waveguide, followed by a 50-cm Hi-1060 fiber selected for optimal pulse compression, maximizing SC broadening after waveguide propagation.

For precise temporal synchronization, an oscilloscope (PicoScope 9402 - 5 GHz) is initially placed after the 50 cm-long single-mode fiber (Thorlabs - HI1060) to tune the time delay using an electrical delay line (i.e., leveraging synchronous oscillators' operation from a common frequency reference - Menlo ASOPS with a phase locked loop based on a Stanford Research Systems FS752 GNSS reference), achieving synchronization within a few tens of picoseconds. Once a coarse synchronization is established, the oscilloscope is removed, and both pulses are injected into the waveguide. The time delay between the pulses is then finely adjusted using an optical spectrum analyzer (OSA, Anritsu MS9710B, 600–1750 nm range). The broadest supercontinuum spectrum generated serves as a temporal reference, with delay optimization refined to a precision of 100 fs (using synchronized and actively-stabilized oscillator repetition rates). After achieving

both spatial and temporal synchronization, we conduct a 15-ps time sweep centered around the reference time (t_{d} = 0 ps). The offset time t_{offset} between the two pulses is numerically estimated to be approximately 3 ps, ensuring precise temporal synchronization at the waveguide's input.

Figure 2(a) shows the optical spectra at the waveguide's output measured as a function of time delay t_{d} over a wide spectral range. As the delay approaches zero, the strong XPM interaction between the femtosecond pulses at two different wavelengths induces significant frequency shifts, leading to SC enhancement. Close to the zero delay, we observe a pronounced spectral sideband around 722 nm, which we interpret as a characteristic signature of temporal reflection [24]. These findings are further supported by numerical simulations and phase-matching analysis.

3.   Numerical Modeling

To simulate dual-pumping SC generation and temporal reflections within the nonlinear waveguide, we used the scalar generalized nonlinear Schrödinger's equation (GNLSE) in the following form [2]:

$$\frac{\partial A}{\partial z} + \frac{\alpha(\omega)}{2}A - \sum_{n \geq 2}\frac{i^{n+1}}{n!}\beta_n\frac{\partial^n A(z,T)}{\partial T^n} = i\gamma\left(1 + i\tau_0\frac{\partial}{\partial T}\right)\left(A\int_{-\infty}^{\infty}R(T')|A(z, T-T')|^2 dT'\right),$$

(1)

where $A(z,T)$ is the complex amplitude of the pulse propagating in the z direction, T is time in a reference frame moving at the speed of 1560-nm pump pulses, $\alpha(\omega)$ is the frequency-dependent propagation loss, and β_n is the nth derivative of the propagation constant. The nonlinear coefficient $\gamma = 2\pi n_2/(\lambda_0 A_{eff})$ [33] is obtained using $n_2 = 1.15 \times 10^{-19} m^2/W$ for the nonlinear refractive index of the high-index silica glass [22]. The effective area A_{eff} of the fundamental mode was estimated from Fig. 1(c), yielding $\gamma = 250 \ W^{-1}km^{-1}$ (at 1560 nm), a value approximately 125 times larger than that of a standard silica fiber. The temporal derivative of the field envelope on the right side of in Eq. (1) corresponds to the self-steepening effect with its characteristic time scale $\tau_0 = 1/\omega_0$ (ω_0 being the angular frequency at 1560 nm). $R(T) = (1 - f_R)\delta(T) + f_R h_R(T)$ is the nonlinear response, where $h_R(T)$ is the delayed temporal Raman response [30], and f_R the fractional contribution of the Raman effect. We use f_R=0.18, the same value used for a standard silica fiber [33].

We also add quantum noise in our numerical simulations using one photon per mode with a random phase [34]. We averaged the results of five pulses propagating under varying input noise conditions and used the dispersion curve of the TM mode, as was done in the experiment. Additionally, we take into account the insertion and propagation losses, as well as the spectral dip resulting from OH⁻ absorption using a Gaussian filter centered at 1380 nm. Finally, simulations also considered nonlinear propagation into the 50 cm HIN fiber as well as the 25 cm PM pigtail before the integrated waveguide, assuming standard dispersion and nonlinear coefficients for such single-mode fibers [33]. As initial conditions, we consider two Gaussian-shaped pulses, one at 1560 nm with 100 fs full width at half maximum (FWHM), and the second at 1040 nm with 150 fs duration (FWHM), and solve Eq. (1) using

$$A(0,T) = \sqrt{P_1}\exp\left[-\left(\frac{T}{T_1}\right)^2\right] + \sqrt{P_2}\exp\left[-\left(\frac{T-t_o-t_d}{T_2}\right)^2\right]e^{i\Omega T},$$

(2)

where the subscripts 1 and 2 are used for 1560 nm and 1040 nm pulses, respectively, and Ω is the frequency difference between their wavelengths. To ensure temporal synchronization at the waveguide's input, an initial offset time t_o is introduced between the two pulses before they propagate through the coupling fibers, accounting for dispersion effects. This offset compensates for the difference in group velocities as the pulses travel through the 50 cm HIN fiber and the 25 cm PM pigtail fiber. Once synchronization is achieved at the waveguide input, an additional

time delay t_d is introduced between the two pulses to investigate its influence on SC generation and temporal reflections, with a numerical precision of up to 250 fs around the zero delay.
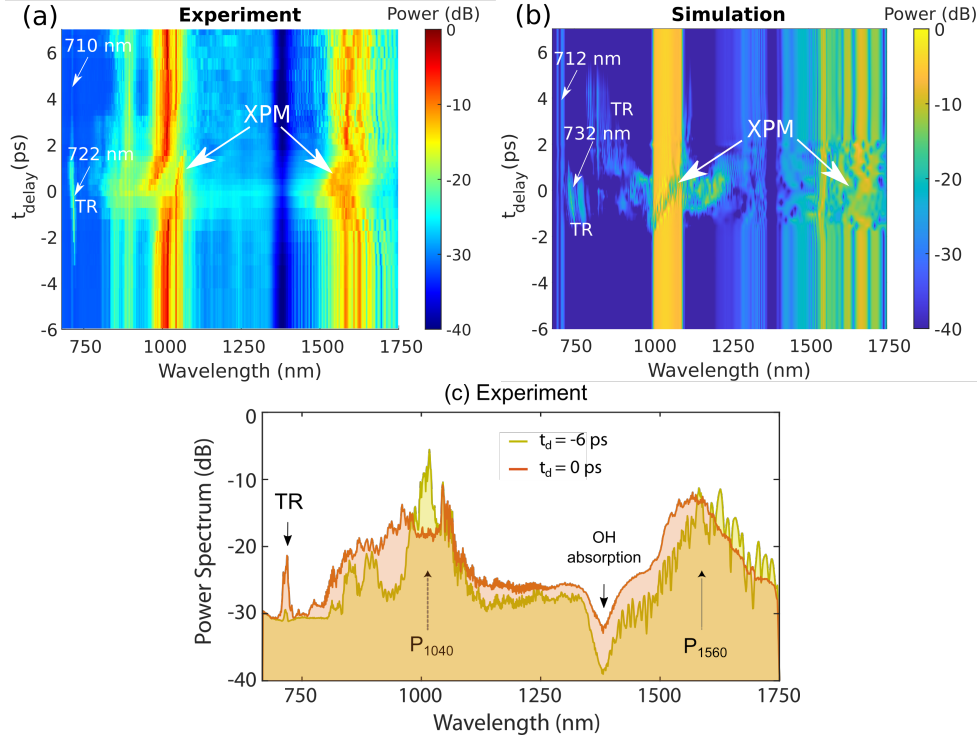

Fig. 2. Dual-pumping on chip SC generation results: Experimental (a) and numerical (b) output optical spectra, displayed in false color, as a function of relative time delay between the two pulses. Both show the XPM-induced wavelength shift and a spectral peak at 722 nm (experiment) and 732 nm (simulations) due to temporal reflections (TR) for small delays. (c) Experimental spectra for two different delays, showing the gain in spectral coverage between 800–1000 nm when t_d= 0 ps and the temporally-reflected radiation at 722 nm (orange spectrum). The dip at 1380 nm is due to water (OH) absorption.

4. Comparison with Numerical Simulations

Figures 2(a) and (b) compare the waveguide's output spectra obtained from experimental measurements and numerical simulations, respectively, as a function of the relative time delay between the two input pulses. Both show the same qualitative features. As the delay becomes small, strong XPM interactions induce significant frequency chirping in both pulses, leading to temporally localized spectral peaks. In addition, a new peak associated with reflection-induced resonant radiation appears around 722 nm in the experiment and 732 nm in numerical simulations. Conversely, another spectral peak is observed at approximately 710 nm in the experiment (and 712 nm in simulations), regardless of the relative time delays. It corresponds to the dispersive wave (DW) generated by the 1560 nm soliton under single-pump conditions. For further visual clarity, we provide in Fig.2(c) a direct comparison of experimental spectra recorded at two different delays. An increase in spectral coverage is observed between 800–1000 nm when the two pulses are synchronized (t_d= 0 ps), along with a blue shift around 1560 nm due to XPM and the temporally-reflected radiation at 722 nm. This translates to an increase in power spectral

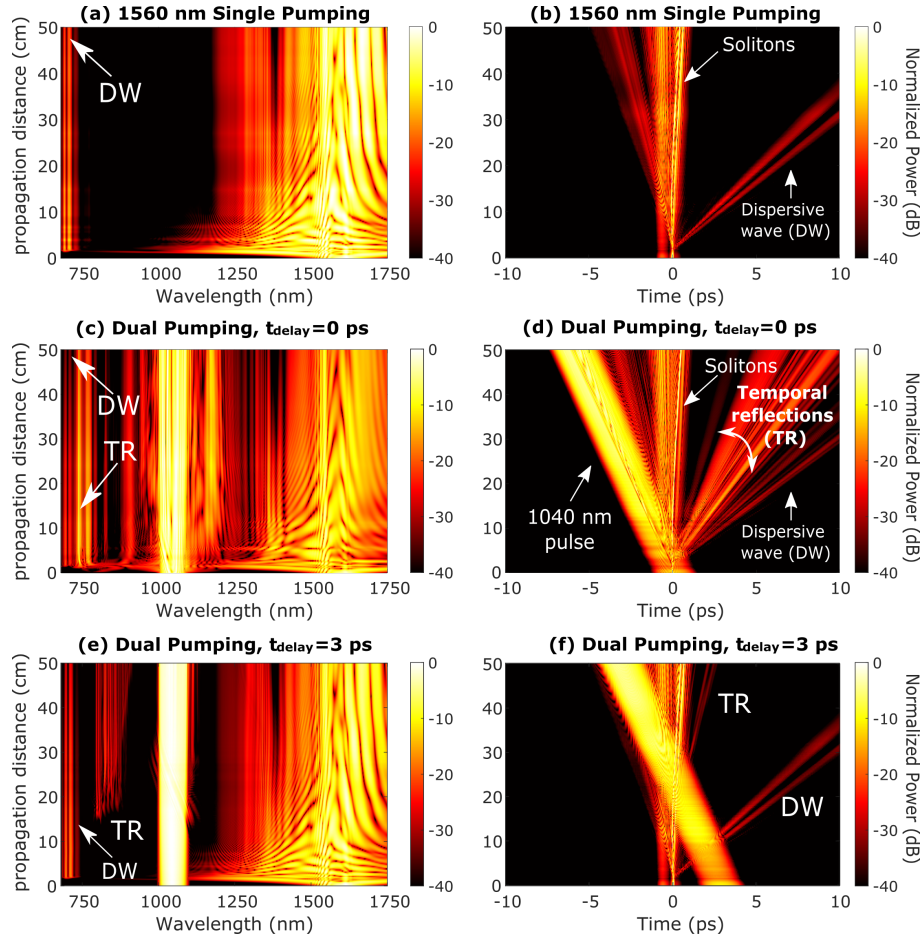density at these wavelengths, while maintaining a constant power budget.

Fig. 3. Numerical Simulations: Spectral (left) and temporal (right) evolution along the chip waveguide. (a,b) Single-pumping case at 1560 nm, showing DW emission around 710 nm from solitons. (c-f) Dual-pumping case showing temporal reflections of the 1040-nm pulse upon its interaction with the 1560-nm soliton index barrier, producing radiation near 722 nm. (c,d) Correspond to a zero relative delay, while (e,f) show the case of +3 ps delay between the two pulses. Two spectrogram videos (See Visualizations 1 and 2) are included as supplementary materials to illustrate temporal reflections at delays of 0 ps and 3 ps, respectively.

To better illustrate the differences between the single and dual pump cases, we show, in Fig. 3, the results of numerical simulations in three cases. The top row shows the spectral and temporal evolution maps when a single pump is used at 1560 nm; the middle and bottom rows show the dual pumping case for relative time delays of 0 and 3 ps, respectively. The corresponding results of the phase-matching analysis are presented in Fig. 4. In the case of a single-pump at 1560 nm, Figs. 3(a-b) reveal the formation, in both the temporal and spectral domains, of a dispersive wave (DW) around 712 nm, generated by the 1560 nm soliton pulse. However, when a 1040 nm pulse is also launched with the 1560 nm pulse with a zero relative delay, a new spectral peak emerges around 732 nm (see Fig. 3(c)). This newly generated wave appears to originate from the temporal reflection of the 1040 nm pulse upon its interaction with the 1560 nm soliton barrier, as shown in

Fig. 3(d). This phenomenon, primarily driven by four-wave mixing interactions between the two pulses, has been theoretically analyzed in Refs. [24, 25]. The formation of the soliton barrier at 1560 nm plays a central role in enabling the temporal reflection process. To quantify this, we numerically estimated the soliton order N at 1560 nm at the waveguide input to be approximately 17. Such a high soliton number explains the strong soliton compression observed in Fig. 3(d), and consequently the multiple temporal reflections experienced by the stretched 1040 nm pulse at the soliton-induced refractive index barrier. To further illustrate temporal reflections in the time–frequency domain, two spectrogram videos corresponding to relative delays of 0 ps and 3 ps are provided as supplementary materials (see Visualizations 1 and 2). Complementarily, Figs. 3(e) and (f) present the effect of introducing a positive relative delay of $t_d = 3$ ps.

5. Phase-Matching Conditions

The wavelength of the dispersive wave emitted by a soliton is known to satisfy the following phase-matching condition [33] :

$$\beta(\omega_{DW}) - \beta(\omega_S) - \beta_1(\omega_{DW} - \omega_S) - \gamma P_S/2 = 0, \tag{3}$$

where ω_{DW} and ω_S represent the DW and soliton angular frequencies, respectively, β_1 is the inverse of the group velocity at ω_S, P_S is the soliton's peak power, and γ is the nonlinear coefficient at 1560 nm. This phase-matching curve is plotted as a red curve in Fig. 4 using the parameter values relevant to our experiments. As seen there, phase matching for the generation of a DW occurs at 712 nm, in good agreement with both our numerical simulations (712 nm) and the experimental spectra shown in Fig. 2 (710 nm).

We next consider the phase-matching condition governing temporal reflections that produce a spectral peak around 732 nm in our experiments. Following the approach in Refs. [25, 26], we use

$$\beta(\omega_{TR} - \omega_S) = \beta(\omega_{1040} - \omega_S), \tag{4}$$

together with

$$\beta(\omega - \omega_S) = \beta(\omega) - \beta_0 - \beta_1(\omega - \omega_S). \tag{5}$$

where ω_{TR} is the angular frequency of the temporally reflected wave, ω_S that of the soliton barrier, and ω_{1040} of the 1040-nm pulse, acting as the probe that undergoes reflection.

The phase-matching condition in Eq. (4) is plotted in Fig. 4 for a pump wavelength of 1560 nm and a probe at 1040 nm, predicting a temporally reflected (TR) wave at 732 nm. This prediction is in excellent agreement with our numerical simulations at zero delay. However, owing to a relatively broad soliton spectrum, its spectral recoil, and a continuous red-shift of the soliton from intrapulse Raman scattering, frequency shifts of temporally reflected waves span a wide range. As seen in Fig. 4, multiple temporal reflections occur, each exhibiting progressively shorter frequency shifts as the optical delay increases up to +5 ps. In contrast, no TR waves are observed for negative delays, as the two pulses do not interact.

6. Stability analysis

We employed the dispersive Fourier transform (DFT) technique to investigate the stability of SC generation under dual pulse femtosecond pumping [35]. This method enables real-time, pulse-to-pulse SC spectral measurements in the time domain by temporally stretching the pulse using a normal dispersion fiber such that its stretched temporal profile mimics its spectrum. In our experiment, we utilized a dispersion compensating fiber (DCF) with a net dispersion of −420 ps/nm over its length with 3.8-dB insertion loss at 1560 nm. At the DCF output end, the temporally stretched spectrum was measured in real time through ultrafast detection systems, ensuring adequate temporal resolution for the time-frequency mapping associated
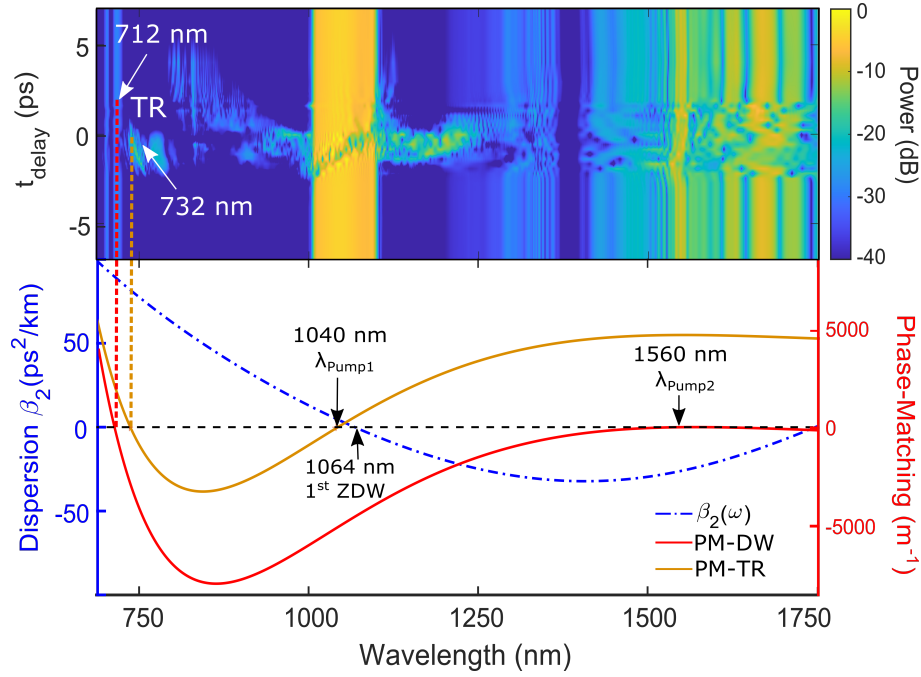
Fig. 4. Top: Numerically-simulated SC spectra as a function of relative time delay between the two pulses at 1040 nm and 1560 nm. Bottom: Dispersion curve (left axis, blue curve) and two phase-matching curves (right axis): (i) peak at 732 nm from temporal reflection (yellow curve) and (ii) peak at 712 nm from DW emission by the 1560-nm soliton (red curve).

with the DFT measurement technique. Here, we used a 5-GHz InGaAs biased photodiode (Thorlabs, DET08CFC/M) connected to a 6-GHz Real-Time Oscilloscope (RTO, Rohde & Schwarz, RTO2064). The RTO is synchronized with an external clock reference at 10 MHz (Stanford Research Systems FS752) that was also driving the input laser oscillator used as an RTO signal trigger. Together, this detection scheme allowed us to measure the DFT spectra with 200 ps resolution (at 20 GSa/s) and minimal jitter, yielding an equivalent spectral resolution of 0.48 nm for real-time DFT measurements (and an equivalent spectral sampling rate of 0.12 nm per point). A spectral filter was applied to isolate the 1560-nm pulse and to prevent any overlap with the 1040-nm pulse. The stretched pulses at a 50-MHz repetition rate were recorded using our fast photodiode. By systematically adjusting the relative time delay between the two pulses, we analyzed the impact of temporal synchronization on SC stability.

Figures 5(a) and (b) present the spectral and relative intensity noise (RIN) measurements, illustrating how the supercontinuum (SC) stability varies with the relative time delay between the pump and probe pulses. Notably, at zero delay ($t_d = 0$), the SC exhibits significantly higher RIN values across a broad spectral range. Here, RIN is defined as the ratio of the standard deviation to the mean of the SC ensemble [36]. We attribute this noise increase primarily to XPM combined with timing jitter. Specifically, the timing jitter between the laser pulses disrupts perfect synchronization and amplifies nonlinear fluctuations. As the relative delay increases, the RIN decreases markedly, indicating improved SC stability. Even a small delay of 0.5 ps produces a noticeable reduction in noise, and by approximately 4 ps delay (Fig. 5(b)), the SC becomes significantly more stable. These results underscore the critical role of temporal synchronization in managing noise and enhancing SC coherence.
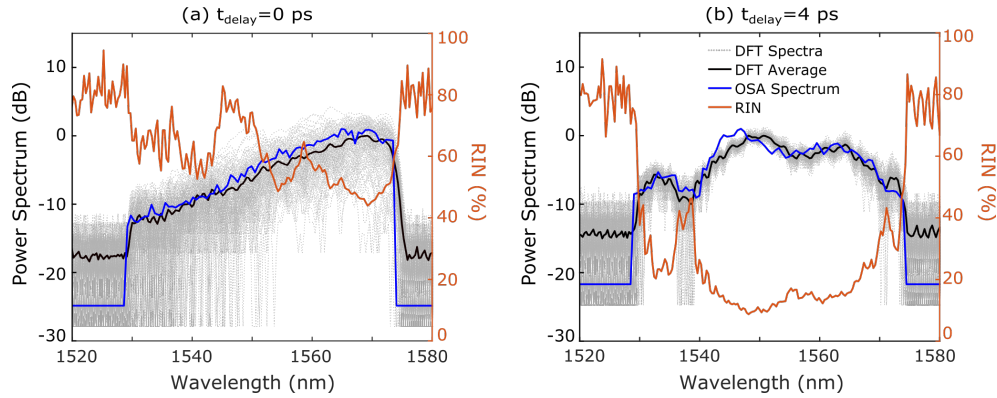
Fig. 5. Real-time pulse-to-pulse spectral measurements using dispersive Fourier transform (DFT) at wavelengths near 1560 nm. Recorded spectra of multiple pulses (light gray), averaged spectrum (black), OSA-measured spectrum (blue), relative intensity noise (RIN, orange) for two relative time delays t_d between the pump-probe pulses.

7. Conclusion

In conclusion, we have investigated dual-pump supercontinuum generation in a photonic integrated circuit and analyzed the impact of different relative time delays between the 1560-nm and 1040-nm pulses. More specifically, we studied the role of cross-phase modulation (XPM) and temporal reflections in enhancing the SC bandwidth. Both numerical simulations and experimental results confirm the occurrence of temporal reflections, occurring when the 1040-nm pulse interacts with the 1560-nm soliton barrier, leading to distinct spectral signatures, in very good agreement with phase-matching considerations. Additionally, a noise analysis based on the dispersive Fourier transform revealed that SC generation becomes unstable and noisy when the two pulses are synchronized, but even a small relative delay between the two pulses significantly improves the SC stability. These findings provide valuable insights into optimizing dual-pump SC generation based on temporal reflections and cross-phase modulation, paving the way for advanced applications in integrated photonics.

8. Acknowledgments

9. Disclosures

The authors have no conflicts of interest to declare.

References

1. R. R. Alfano, *The supercontinuum laser source, 4th ed.* (Springer Nature, 2023).
2. J. M. Dudley and J. R. Taylor, *Supercontinuum generation in optical fibers* (Cambridge University Press, 2010).
3. C. Poudel and C. F. Kaminski, "Supercontinuum radiation in fluorescence microscopy and biomedical imaging applications," J. Opt. Soc. Am. B **36**, A139–A153 (2019).
4. T. Udem, R. Holzwarth, and T. Haensch, "Optical frequency metrology," Nature **416**, 233–7 (2002).

5. E. S. Lamb, D. R. Carlson, D. D. Hickstein, *et al.*, "Optical-frequency measurements with a Kerr microcomb and photonic-chip supercontinuum," Phys. Rev. Appl. **9**, 024030 (2018).

6. A. Manninen, T. Kääriäinen, T. Parviainen, *et al.*, "Long distance active hyperspectral sensing using high-power near-infrared supercontinuum light source," Opt. Express **22**, 7172–7177 (2014).

7. T. Sylvestre, E. Genier, A. N. Ghosh, *et al.*, "Recent advances in supercontinuum generation in specialty optical fibers," J. Opt. Soc. Am. B **38**, F90–F103 (2021).

8. C.-S. Brès, A. D. Torre, D. Grassani, *et al.*, "Supercontinuum in integrated photonics: generation, applications, challenges, and perspectives," Nanophotonics **12**, 1199–1244 (2023).

9. D. Moss, R. Morandotti, A. Gaeta, and M. Lipson, "New cmos-compatible platforms based on silicon nitride and hydex for nonlinear optics," Nat. Photonics **7**, 597–607 (2013).

10. H. Guo, C. Herkommer, A. Billat, *et al.*, "Mid-infrared frequency comb via coherent dispersive wave generation in silicon nitride nanophotonic waveguides," Nat. Photonics **12**, 330–335 (2018).

11. D. Y. Oh, D. Sell, H. Lee, *et al.*, "Supercontinuum generation in an on-chip silica waveguide," Opt. Lett. **39**, 1046–1048 (2014).

12. D. Duchesne, M. Peccianti, M. R. E. Lamont, *et al.*, "Supercontinuum generation in a high index doped silica glass spiral waveguide," Opt. Express **18**, 923–930 (2010).

13. N. Singh, M. Xin, D. Vermeulen, *et al.*, "Octave-spanning coherent supercontinuum generation in silicon on insulator from 1.06 µm to beyond 2.4 µm," Light. Sci. & Appl. **7**, 17131–17131 (2018).

14. R. Halir, Y. Okawachi, J. S. Levy, *et al.*, "Ultrabroadband supercontinuum generation in a cmos-compatible platform," Opt. Lett. **37**, 1685–1687 (2012).

15. A. R. Johnson, A. S. Mayer, A. Klenner, *et al.*, "Octave-spanning coherent supercontinuum generation in a silicon nitride waveguide," Opt. Lett. **40**, 5117–5120 (2015).

16. C. Lafforgue, S. Guerber, J. M. Ramírez, *et al.*, "Broadband supercontinuum generation in nitrogen-rich silicon nitride waveguides using a 300 mm industrial platform," Photonics Res. **8** (2020).

17. M. Sinobad, C. Monat, B. Luther-Davies, *et al.*, "Mid-infrared octave spanning supercontinuum generation to 8.5 μm in silicon-germanium waveguides," Optica **5** (2018).

18. M. Montesinos-Ballester, C. Lafforgue, J. Frigerio, *et al.*, "On-Chip Mid-Infrared Supercontinuum Generation from 3 to 13 μm Wavelength," ACS photonics **7**, 3423–3429 (2020).

19. K. Hammani, L. Markey, M. Lamy, *et al.*, "Octave spanning supercontinuum in titanium dioxide waveguides," Appl. Sci. **8** (2018).

20. M. R. Lamont, B. Luther-Davies, D.-Y. Choi, *et al.*, "Supercontinuum generation in dispersion engineered highly nonlinear (γ = 10 /w/m) As$_2$S$_3$ chalcogenide planar waveguide," Opt. Express **16**, 14938–14944 (2008).

21. K. F. Fiaboe, A. D. Torre, A. Mitchell, *et al.*, "Design of Mid-Infrared Supercontinuum Generation in a strip-loaded LNOI Waveguide through lateral leakage engineering," in *European Conference on Integrated Optics,* (Enschede, Netherlands, 2023).

22. G. Li, Y. Li, F. Ye, *et al.*, "Supercontinuum Generation in Dispersion Engineered Highly Doped Silica Glass Waveguides," Laser Photonics Rev. **17**, 2200754 (2023).

23. G. Granger, M. Bailly, H. Delahaye, *et al.*, "Gaas-chip-based mid-infrared supercontinuum generation," Light. Sci. Appl. **12** (2023).

24. B. Plansinis, W. Donaldson, and G. Agrawal, "What is the temporal analog of reflection and refraction of optical beams?" Phys. Rev. Lett. **115**, 183901 (2015).

25. K. Webb, M. Erkintalo, Y. Xu, *et al.*, "Nonlinear optics of fibre event horizons," Nat. communications **5** (2014).

26. C. Ciret, F. Leo, B. Kuyken, *et al.*, "Observation of an optical event horizon in a silicon-on-insulator photonic wire waveguide," Opt. Express **24**, 114–124 (2016).

27. T. Schreiber, T. V. Andersen, D. Schimpf, *et al.*, "Supercontinuum generation by femtosecond single and dual wavelength pumping in photonic crystal fibers with two zero dispersion wavelengths," Opt. Express **13**, 9556–9569 (2005).

28. E. Räikkönen, G. Genty, O. Kimmelma, *et al.*, "Supercontinuum generation by nanosecond dual-wavelength pumping in microstructured optical fibers," Opt. Express **14**, 7914–7923 (2006).

29. P.-A. Champert, V. Couderc, P. Leproux, *et al.*, "White-light supercontinuum generation in normally dispersive optical fiber using original multi-wavelength pumping system," Opt. Express **12**, 4366–4371 (2004).

30. C. Khallouf, V. T. Hoang, G. Fanjoux, *et al.*, "Supercontinuum generation in high-index doped silica photonic integrated circuits under diverse pumping settings," Opt. Express **33**, 8431–8444 (2025).

31. G. Li, Y. Li, F. Ye, *et al.*, "Supercontinuum Generation in Dispersion Engineered Highly Doped Silica Glass Waveguides," Laser & Photonics Rev. **17**, 2200754 (2023).

32. M. Zerbib, V. Hoang, J. Beugnot, *et al.*, "Observation of Brillouin scattering in a high-index doped silica chip waveguide," Results Phys. **52**, 106830 (2023).

33. G. P. Agrawal, *Nonlinear Fiber Optics, 6th ed.* (Elsevier & Academic Press, 2019).

34. E. Genier, P. Bowen, T. Sylvestre, *et al.*, "Amplitude noise and coherence degradation of femtosecond supercontinuum generation in all-normal-dispersion fibers," J. Opt. Soc. Am. B **36**, A161–A167 (2019).

35. T. Godin, L. Sader, A. K. Kashi, *et al.*, "Recent advances on time-stretch dispersive Fourier transform and its applications," Adv. Physics: X **7**, 2067487 (2022).

36. E. Genier, S. Grelet, R. D. Engelsholm, *et al.*, "Ultra-flat, low-noise, and linearly polarized fiber supercontinuum

source covering 670–1390 nm," Opt. Lett. **46**, 1820–1823 (2021).